Association Aéronautique et Astronautique de France

57th 3AF International Conference on Applied Aerodynamics
29 — 31 March 2023, Bordeaux – France

AERO2023-15-HART

Thrust/Drag Decomposition using Partial Pressure Fields

Pierce L. Hart[(1)], Ngonidzashe E. Mutangara [(2)], Drewan S. Sanders [(3)] and Sven Schmitz [(4)]

[(1)] *The Pennsylvania State University, University Park, PA, 16802, United States of America, puh69@psu.edu*

[(2)] *Cranfield University, Cranfield, MK43 0AL, United Kingdom, ngonidzashe.e.mutangara@cranfield.ac.uk*

[(3)] *Cranfield University, Cranfield, MK43 0AL, United Kingdom, d.s.sanders@cranfield.ac.uk*

[(4)] *The Pennsylvania State University, University Park, PA, 16802, United States of America, sus52@psu.edu*

ABSTRACT

The accurate prediction of aircraft performance requires a robust definition of thrust/drag accounting. Traditional nacelle-pylon configurations have been treated as separate entities which are combined linearly; however, this is not feasible for embedded propulsion systems which have a higher degree of interaction than traditional designs. With the apparent shift to embedded propulsion systems in the N+3 generation of aircraft, of which boundary-layer ingestion technology is a driving factor, improving our understanding of propulsion system interactions with an air-frame has never been more important. Since many of these interactions occur close to the body, a near-field decomposition method, partial pressure fields, is employed in CFD to provide insight as to the interactive aerodynamics of an embedded propulsion system.

1. INTRODUCTION

The motivation for drag decomposition has been to offer insight as to the sources of drag on an aerodynamic body, equipping an aircraft designer with sufficient information to make informed decisions regarding design considerations.

Drag decomposition analysis originates from Prandtl's lifting-line theory in which the induced drag of a wing can be predicted using a mathematical model [1]. Betz, who made significant contributions to Prandtl's work, then proposed a real-world method of identifying profile drag using wind tunnel measurements, the first of its kind [2]. This work was furthered by Jones [3], before Oswatitsch proposed a decomposition of profile drag using entropy [4]. In 1972, Maskell developed an augmented formula for induced drag compared to the original one proposed by Betz, the complement to profile drag decomposition [5]. Thus, a foundation for drag decomposition studies was created.

The introduction and development of CFD software, which has been established as a cost-effective supplement to wind-tunnel testing, has been highly influential on the direction of drag decomposition research. Steger and Baldwin [6] were the first to implement a decomposition in CFD, where wave drag was evaluated in inviscid flow using Oswatitch's formulation. Yu et al. [7] then attempted a decomposition of both induced and wave drag; however, a discrepancy between classical far-field wake measurements and the near-field method led to their efforts being abandoned. Lock [8] addressed this discrepancy and brought forth the concept of spurious drag, defined as the artificial drag created as a result of truncation error, numerical error, and artificial dissipation in numerical simulations. The concept of spurious drag remains an active topic of discussion [9, 10, 11].

While there are drawbacks to computational methods, the prominence of data throughout the flow field has allowed for significant developments in accounting of drag sources. One of the most significant breakthroughs has been the decomposition of profile drag into viscous and wave drag [12, 13] components using volumetric filtering. Furthermore, alternative decomposition methods have been developed, such as the vortex–force method [14], power balance [15] and exergy methods [16], and partial pressure fields [17].

Unfortunately, methods do not perform consistently in power-on considerations. Some traditional far-field methods have accounted for the enthalpy of the propulsion system [18, 19] which allowed Destarac & van der Vooren to perform a thrust/drag analysis for a commercial transport aircraft [20]. Entrainment limits the usefulness

of these traditional far-field methods to conventional nacelle/pylon propulsion systems.

There has, however, been a desire to better understand the flow interactions of an embedded propulsion system. A large driving factor in adequately decomposing these configurations has been the re-emergence of boundary-layer ingestion (BLI) technology in modern aircraft design [21, 22, 23]. The concept of using the boundary-layer to improve aircraft fuel economy was originally proposed in the 1940's with the breakthrough study of Smith & Roberts [24], suggesting that the propulsion system can be designed to reduce drag by using low momentum air while adequately controlling the boundary-layer to reduce skin friction drag. The principle was applied to naval architecture [25, 26, 27], yet remained unused in the world of aircraft design. That was until the turn of the millennium when the concept gained attention as a way to improve fuel efficiency. Various improvements in efficiency were reported using a variety of metrics [28, 29, 30, 31], yet there appears to be a limited understanding as to the secondary effects of BLI technology.

This provided motivation for Drela to develop the power balance method [15] which overcomes entrainment issues through analysis of the mechanical energy equation, hence providing a means of performance accounting for embedded propulsion systems. This method was furthered by Arntz to allow one to consider both thermodynamic and mechanical effects. As a result, these methods have been deemed the industry standard, and have been further developed and analyzed to best predict the efficiency of a given configuration [32, 33, 34], providing further insight as to the accounting of thrust and drag sources as well as their interactions.

While such methods are beneficial to our understanding of highly integrated propulsion systems, there are still aspects of thrust/drag book-keeping that remain unclear. In order to better understand this, various issues associated with thrust/drag book-keeping are summarized. Separation of the lifting body into internal and external regions is a major proponent of these decompositions, which is traditionally separated by a stagnation streamline. However, such a split is counterintuitive as the external and internal components are highly interactive, with a change in external flow impacting the internal flow and vice versa. Further to this, the propulsion and aerodynamic interactions greatly influence the flow upstream, with the resultant change in drag sometimes referred to as additive or secondary drag. Finally, the definition of thrust itself is unclear, whether this is the net force generated within the internal flow region or simply the thrust added to the flow itself.

Arntz's exergy methodology offers perspective and detail on the sources of thrust and drag while utilizing traditional book-keeping convention. Nevertheless, if one is to further our understanding of the flow field interactions induced by a propulsor, a near-field analysis is essential. Current understanding of the near field is limited to visualizing the change in flow-fields between power-off and power-on states, which provides limited insight. It therefore would be logical to perform a near-field drag decomposition, with the only current known methodology being partial pressure fields (PPFs).

The concept of PPFs was initially developed by Schmitz & Coder [17] for incompressible flows. Schmitz then extended this work to include compressibility effects [35], which was then applied to various aerodynamic bodies by Hart & Schmitz [36, 37]. PPFs decompose drag through splitting the linear pressure term and isolating components of the Navier-Stokes equations. Thus far that has been to isolate the Euler pressure associated with lift and shockwaves and the dissipative pressure which sums with the skin friction to determine the viscous drag. The resulting decomposition has proven to agree well with far-field methods. PPF methods have also been extended to account for wave drag sources [38, 39].

In the present paper, an extension of PPFs is developed to improve our understanding of thrust and drag sources. The highly interactive nature of BLI, and the desire to further our understanding of the technology and its limitations, makes for a perfect case study. For this reason, the configuration chosen for analysis is the 2D NACA 23012 airfoil interacting with a Clark-Y airfoil scaled to 13% of the size of the main element. This aerodynamic body was initially analysed by Arntz & Atinault [40]. PPF theory is first summarized and then extended to account for a propulsive momentum source in Section 2. Numerical methods are discussed and the grid creation and solver used are detailed, along with the actuator disk model that is used to emulate an infinitely thin blade, in Section 3. The results of the case study are presented in Section 4, with conclusions on the findings presented in Section 5.

2. PARTIAL PRESSURE FIELDS

Partial pressure field theory was developed as an alternative means of decomposition to far-field methods. The decomposition is solved directly by isolating terms of the Navier-Stokes equations. Thus far, decompositions have been limited to the most basic form of the Navier-Stokes equation with no external body forces, volumetric heat generation, or heat conduction:

$$\nabla \cdot (\rho \mathbf{q}\mathbf{q}) = -\nabla p + \nabla \cdot \tau \tag{1}$$

Here ρ is the local fluid density, $\mathbf{q}$ is the velocity vector, p is the local fluid pressure, and τ is the viscous stress tensor. A decomposition is realized by splitting static pressure into a dissipative partial pressure, p_μ, and a corresponding Euler pressure, p_E. These 'partial pressures'

are grouped with associated terms, i.e., the Euler pressure gradient with the convective acceleration term, and the dissipative PPF balances the transport of the viscous stresses in the flow field.

$$[\nabla \cdot (\rho \mathbf{qq}) + \nabla p_E] + \left[-\nabla \cdot \tau + \nabla p_\mu\right] = 0 \tag{2}$$

In powered conditions, the added thrust term can be represented as a momentum source term, S_ϕ, and the momentum equation can be rewritten:

$$\nabla \cdot (\rho \mathbf{qq}) = -\nabla p + \nabla \cdot \tau + S_\phi \tag{3}$$

Here the linearity of pressure allows for an additional split of the pressure term, where the new decomposition is

$$[\nabla \cdot (\rho \mathbf{qq}) + \nabla p_E] + \left[-\nabla \cdot \tau + \nabla p_\mu\right] + \left[\nabla p_{S_\phi} - \mathbf{S}_\phi\right] = 0 \tag{4}$$

A pressure decomposition is realized by isolating each component and equating the gradients to zero, which satisfies the Euler-momentum equation, and there is zero dissipative pressure, p_μ, in the event that there are no viscous stresses. Furthermore, there is the added assumption that no pressure due to thrust, p_{S_ϕ}, is generated when there is no momentum source in the flow field. The equations were coded using a Poisson solver with appropriate boundary conditions defined as outlined by Schmitz [35] and Hart & Schmitz [36].

Boundary conditions are defined in the far field where the viscous effects tend to zero, i.e., $p_\mu = 0$ at inlets and sides. Meanwhile, Euler and propulsive pressure have a zero-flux condition, $\nabla p_E = 0$ and $\nabla p_{S_\phi} = 0$. At the outlet, a Neumann boundary condition exists for all PPFs, in which the pressure gradient normal to the outlets is zero, for dissipative pressure this would be $\nabla p_\mu \cdot \mathbf{n} = 0$. At the walls, $\nabla p_\mu = \nabla \cdot \tau$ and $\nabla p_{S_\phi} = S_\phi$, while the no-slip condition results in a zero-flux Euler pressure boundary condition.

3. NUMERICAL METHODS

Simulations were performed on the 2D aerodynamic body, which consists of a main element NACA 23012 airfoil that is unit chord length, and a Clark-Y airfoil scaled to 13% of the size. The Clark-Y is located aft on the upper surface of the NACA 23012 airfoil, it is rotated and anchored at its trailing edge, which shares the same streamwise location as the main element. A structured grid was created using CFD guidelines, i.e., a leading edge and trailing edge spacing of 0.1% and 0.05% of a given elements chord length. Initial wall spacing, y^+, a highly influential parameter in near-field decompositions [36], was maintained below a value of 0.5. There are 825 wrap around points on the NACA 23012 airfoil and 870 on the Clark-Y airfoil, with the channel between the two airfoils having a 200×300 domain. In total, the mesh contains 750,000 cells, which was deemed sufficient to accurately capture the drag sources required for both a near-field and far-field decomposition. Processing was undertaken on ANSYS Fluent's 2022R1 pressure-based solver. Simulations were performed using pressure–velocity coupling with second-order upwinding implemented to calculate all numerical fluxes, including PPFs, and gradients were evaluated using the Green–Gauss cell-based method. Turbulence was modeled using the Spalart–Allmaras one-equation model. PPFs were derived using the methodology outlined by Hart & Schmitz [36].

The propulsion system is modelled as an actuator disk which acts as an infinitely thin propeller, details of which are covered by Schmitz [41]. This can be implemented in a CFD solver through use of momentum and energy source terms. The present case study considers a momentum source placed near the midpoint of the Clark-Y airfoil, in line with the study of Arntz & Atinault. All power-on configurations are considered 'in-trim' where thrust and drag are balanced. Since these terms are coupled, a force balance requires the Navier-Stokes to be resolved iteratively from a power-off condition until the near-field drag reconverges in a power-on state.

For the purposes of this study, two types of disk model are used, as highlighted in Fig. 1. The equal-weighted step adds a constant thrust per cell, achieved by dividing the input force by the sum of the cell volumes on which the source term is acting. The source term per cell in-trim is therefore defined as:

$$S_\phi = D/\Sigma V \tag{5}$$

A Gaussian distribution is also used, which weighs the strength of the source terms relative to the distance from the blade. The weight of each cell, η, is incorporated and the source term is written as:

$$S_\phi = D\eta/\Sigma \eta V \tag{6}$$

In order to ensure the propulsion system is as realistic as possible, the momentum source is projected normal to the disk. Since cases are in trim, the X-momentum source term is maintained at a unit value. Upon volumetric integration of this source term, one can calculate thrust. Meanwhile, a Y-momentum source is added to direct the flow. The energy term is the resulting velocity dot product with the momentum sources.

4. RESULTS

The first steps in performing a valid thrust/drag decomposition are to consider the variance of momentum source models. In this study, the results of a step function and

Figure 1: Actuator Disk Models.

Gaussian distribution are compared and the distribution of momentum can be visualized in Fig. 1. The results of a drag decomposition comparison in subsonic flow are shown in Tab. 1. There is minimal discrepancy between the total drag, c_d , between the models used. Even a classical near-field decomposition (pressure drag, c_{d_p} , + skin friction drag, c_{d_τ}) shows strong agreement; however, a PPF decomposition shows a larger fluctuation between drag sources. For the purposes of this paper, the Gaussian distribution is used. In general, the results show the influence an actuator disk model has on thrust/drag bookkeeping.

Table 1: Comparison of Resulting Drag Decomposition using Gaussian & Step Function Actuator Disk Models ($M_\infty = 0.2$, $Re = 4.36 \times 10^6$).

$c_d \times 10^4$:	c_d	c_{d_p}	c_{d_τ}	$c_{d_{p_\mu}}$	$c_{d_{p_E}}$	$c_{d_{ps_\phi}}$
Gaussian	135.7	53.2	82.5	13.4	39.6	0.2
Step	135.5	52.9	82.5	10.7	42.3	-0.1

The case study is validated by comparing results to the initial work of Arntz & Atinault [40], see Tab. 2. A comparison of unpowered and powered cases is made at three flow conditions, while angle of attack is maintained at zero degrees, in line with the case study. These conditions represent the array of flight conditions that BLI may operate at for commercial transport aircraft. As such, Mach numbers varies from subsonic flow ($M_\infty = 0.2$) to transonic flow ($M_\infty = 0.7$). Furthermore, Reynolds number is also varied from 4.36 million to 9.95 million, and up to 12.62 million in transonic flow. Data agrees well under power-off conditions in the subsonic regime, with a discrepancy between the two studies being no larger than 3 drag counts. In transonic flow, this increases to 11 counts, which is significantly larger; however, in this case, shocks form on both lifting bodies, with shock-induced stall occurring on the Clark-Y airfoil. Given all other assumptions that are not accounted for in terms of computational grids and exact positioning of the Clark-Y airfoil, such a discrepancy between case studies is acceptable. Comparing power-on data becomes intricate because Arntz defines internal and external flow, where the internal component of drag is essentially ignored. For the purposes of this study, such a distinction is only used to compare results to Arntz. An external definition is used based on the Gaussian distribution spreading. As in the power-off cases, both subsonic data sets match closely to Arntz data, but the transonic case is predicting a higher drag than that of Arntz. Considering the complex flow interactions, the agreement in total drag between studies is deemed sufficient and provides a valid basis for PPF decomposition. As mentioned earlier, there is a lack of sufficient information regarding the geometry mesh and flow modelling, which makes for the discrepancy in total drag values more acceptable.

Table 2: Comparison of Drag Balance to Arntz & Atinault [40].

$c_d \times 10^4$:	c_d − Unpowered		c_d − Powered		
	Total	Arntz	Total	External	Arntz
$M_\infty = 0.2$	112	110	135.7	112.1	110
$M_\infty = 0.5$	106.6	104	129.9	105.5	104
$M_\infty = 0.7$	199	188	243.9	231	210

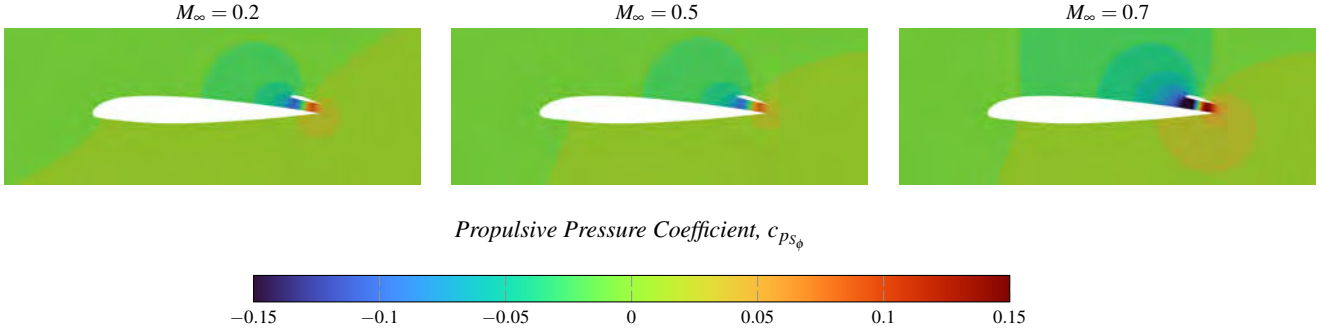

Figure 2: Propulsive Pressure Field acting around the Aerodynamic Body at Various Mach Numbers.

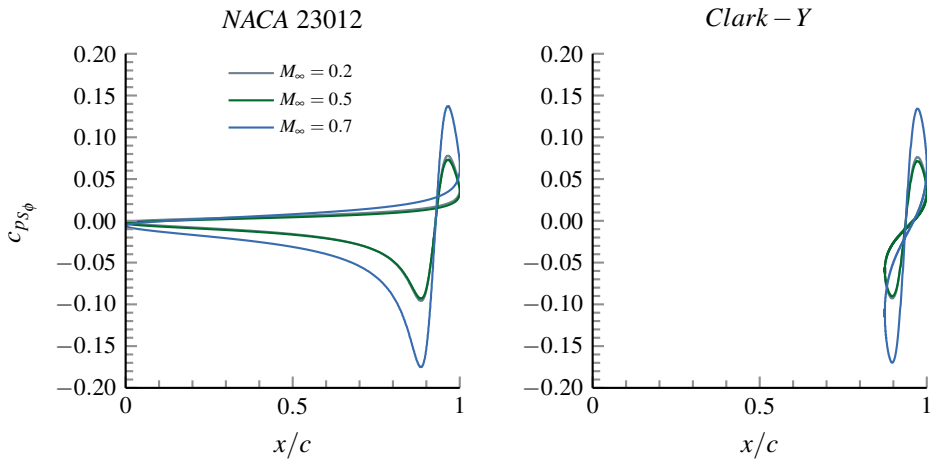

Figure 3: Propulsive Pressure, c_{ps_ϕ}, on Aerodynamic Surface at Various Mach Numbers.

A general observation that can be made from the total drag measurements in Tab. 2 is that in power-on configurations, the presence of drag sources increases due to interactions with the propulsor. This is most prominent for the transonic case where there is an added disturbance of shockwaves to consider. In order to better understand the changes in drag, a PPF decomposition is conducted. First, the propulsive pressure field, c_{ps_ϕ}, is visualized, see Fig. 2, where the propulsive PPF acts like a dipole.

The propulsive PPF, c_{ps_ϕ}, accounts for the direct effect of the propulsor on the near-field forces. These pressure fields propagate throughout the entire flow field, and hence disturb the flow. With a pressure coefficient range between 15 percent of the stagnation value, it is apparent that this pressure field has a notable impact on the lift and drag generated. At lower Mach numbers, where the values of thrust produced are similar, the resulting PPFs appear very similar; however, for the transonic case study, the resulting force field produced is greater, with the thrust produced being nearly twice as large. These observations are further supported by comparison of the propulsive PPF surface pressures in Fig 3. The overall size of the transonic pressure field is amplified by a factor of two from the subsonic cases, which correlates with the total thrust produced. With the actuator disk spaced at the midpoint of the Clark-Y, the pressure forces appear to visibly balance each other out in the streamwise direction.

A PPF decomposition is also informative as to the secondary effects of a propulsion system. This is best demonstrated through comparison of the Euler and static pressure fields, shown on the surface of each element at subsonic flow conditions in Fig. 4. In power-off conditions, the static and Euler pressures are in strong agreement, where the Euler pressure, c_{p_E}, captures practically all of lift. The difference between these two is the dissipative pressure, c_{p_μ}, which has a near-zero impact on lift but

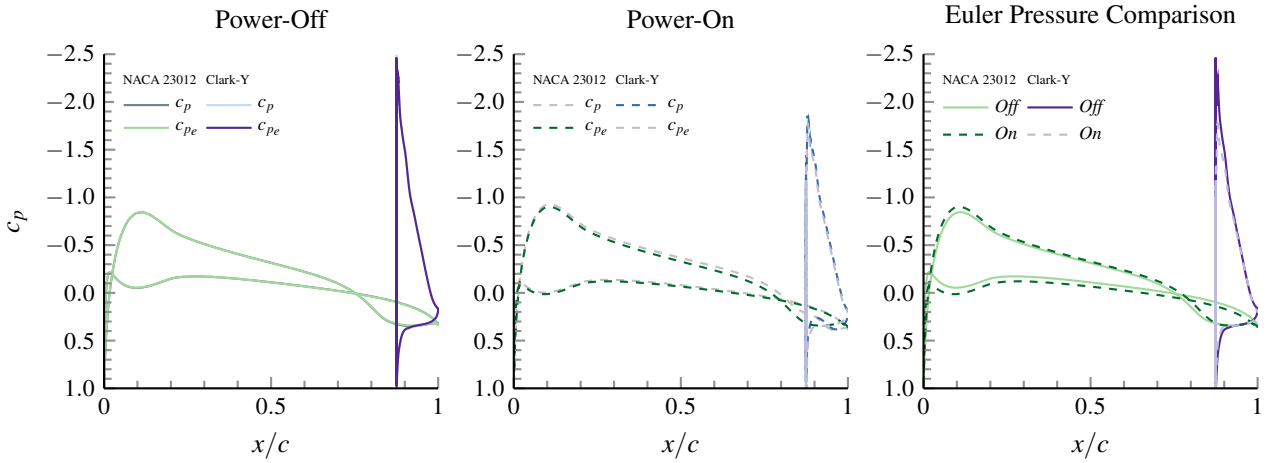

Figure 4: Surface Pressures, c_p & c_{p_e}, Compared at Power-Off & Power-On Conditions ($M_\infty = 0.2$, $Re = 4.36 \times 10^6$).

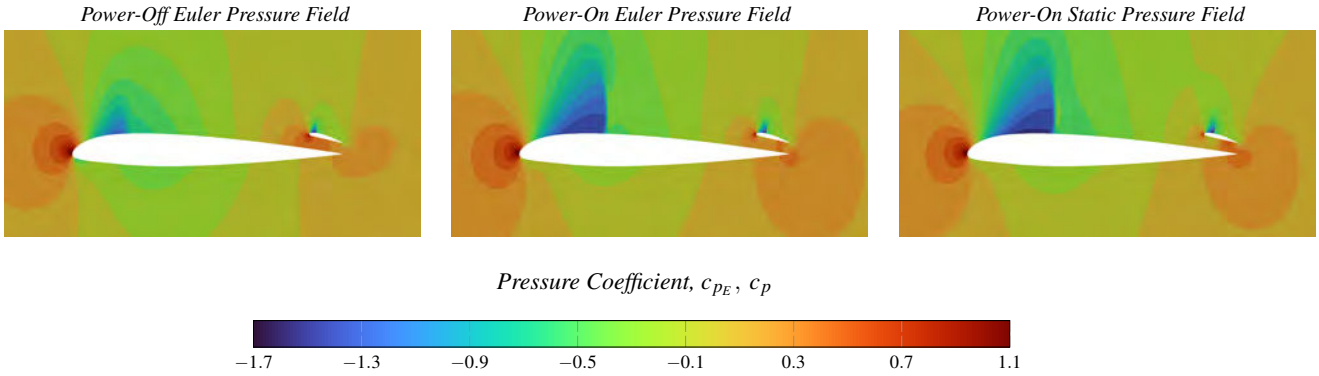

Figure 5: Comparison of Euler Pressure Fields ($M_\infty = 0.7,\ Re = 12.62 \times 10^6$).

captures a notable amount of drag. Under power-on conditions, the additional momentum source term leads to a discrepancy between the static pressure, c_p, and the Euler pressure, c_{p_E}. This difference is most prominent close to the propulsor, $x/c = 0.9$. Instead, the Euler pressure behaves as if there are no gradients added to the flow field. As a result of the isolation of the momentum source, a comparison of the two Euler pressures in Fig. 4 (right) allows for a direct comparison of pressure fields in power-off and power-on conditions, with the difference being the secondary effects related to the Euler pressure, i.e., viscous–inviscid interactions and wave drag effects. In the case of subsonic flow, there is a slight increase in the suction peak height and overall lift on the NACA 23012, while there is a significant reduction in the size of the Clark-Y suction peak. One must note that there is also a change in the dissipative pressure field, which is a contributor to the viscous drag.

A comparison of the Euler pressure scalar fields is equally as revealing as surface pressure data. This is shown for transonic flow, see Fig. 5. One can visually see the significance of the secondary effects of the propulsion system. The change in the size and strength of the shockwaves between the power-off (left) and power-on (middle) cases is apparent. Since shock waves are significant contributors to lift and drag, the distortion of the additive effects the propulsion system has on lift and drag cannot be ignored. A comparison of the Euler pressure field (middle) is made with the static pressure field (right), with the most significant discrepancy occuring in the channel region, where the actuator disk is located, see Fig. 6. A comparison of the two pressure fields within the channel shows the significant pressure field data that is filtered by the Euler pressure field, c_{p_e}.

Just as many of the secondary effects of the propulsion system are visualized by comparing the Euler pressure for power-off and power-on conditions, in Fig. 4 (right), the same can be done using the scalar fields, where the resulting change in Euler pressure is shown in Fig. 7. This allows one to visibly quantify the portions of the additive drag induced by the propulsion system. From the visual, it is clear that the propulsion effects propagate throughout the flow field. There is a change in the pressure gradients at the leading edges of both airfoils as well as in the shock location. Ultimately, the effects of a propulsion system distort the entire flow field.

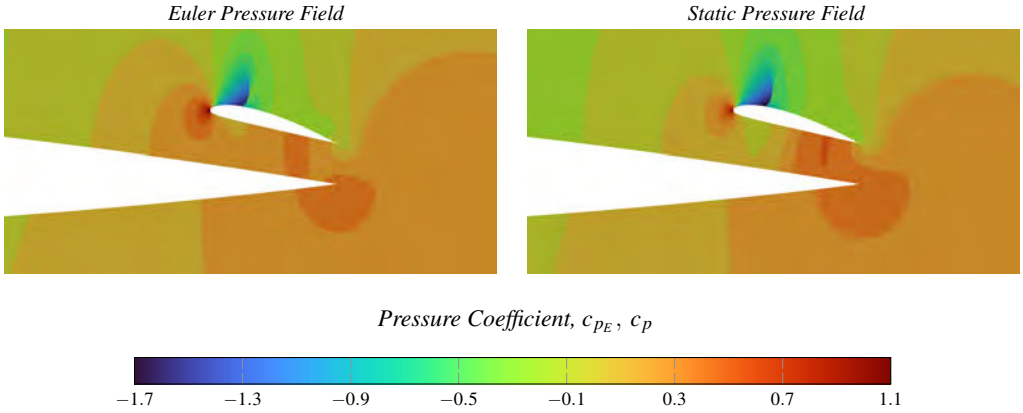

Figure 6: Comparison of Euler, c_{p_e} & Static Pressure, c_p, Fields in Channel under Power-On Conditions ($M_\infty = 0.7,\ Re = 12.62 \times 10^6$).

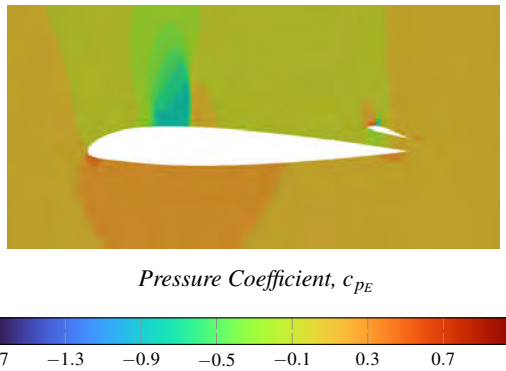

Figure 7: Change in Euler Pressure Field Between Unpowered & Powered Configuration ($M_\infty = 0.7$, $Re = 12.62 \times 10^6$).

While the change in dissipative pressure drag, $c_{d_{p_\mu}}$, is minimal as later discussed, a comparison of dissipative pressure in power-off and power-on conditions in the channel is informative on the dissipative effects of a propulsor. A comparison of these states is made in Fig. 8. Under power-on conditions, the dissipative pressure gradients are more prominent across the channel; this can be observed by the greater change in contour lines. There is an apparent shift in dissipation across the actuator disk as one would expect, while the dissipative pressure gradients around the trailing edge of the Clark-Y appear to be smaller. Overall, PPF theory may provide a designer with valuable information as to the dissipation effects of the actuator disk model and be used for configuration optimization.

The results of a drag decomposition study are presented in Tab. 3. There are several observations to be made from this decomposition study. Starting with the propulsive PPF, $c_{d_{p_{S_\phi}}}$, one can see that the propulsion system has a very small direct impact on the resulting drag of the power-on configuration. This is in large part due to the balancing of forces in the streamwise direction. However, the size of the pressure gradients observed in Fig. 3 suggests that in non-ideal circumstances, i.e., inlet distortion, the resulting pressure-field could in fact be a significant drag contributor.

The propulsive drag produced also scales linearly with the required thrust input, that is the thrust required to overcome drag. For example, the transonic flow case has close to twice the thrust input of the subsonic cases and twice the propulsive drag produced but its very small compared to all other drag sources.

Secondly, one now has a method of quantifying the secondary effects of the propulsion system. The viscous drag, the summation of the dissipative drag and skin friction drag, $c_{d_{p_\mu}} + c_{d_\tau}$, is not impacted all that much by the introduction of a propulsion system. The Euler drag, on the other hand, which carries all of the inertial flow effects, is highly dependent on the propulsor activity. The resulting Euler drag, $c_{d_{p_E}}$ is by far the largest contributor of secondary effects. Secondary drag values of each grouping are determined by taking the difference of their respective drag groupings between the power-off and power-on states.

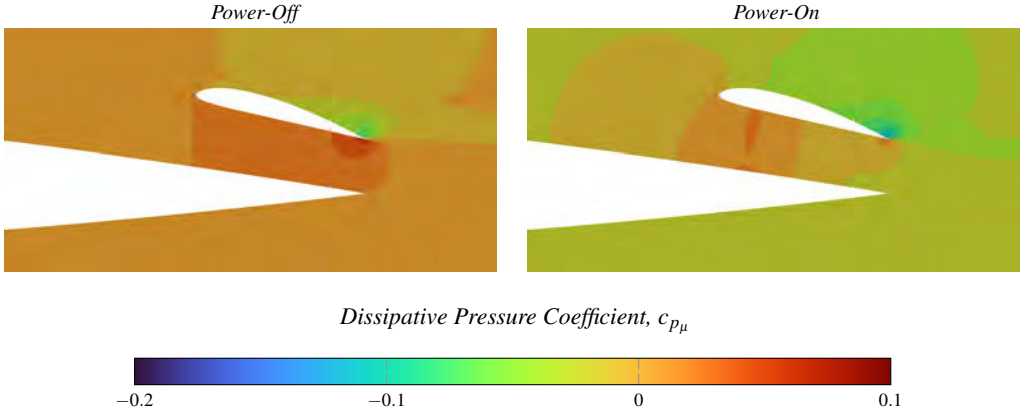

Figure 8: Comparison of Dissipative Pressure Field at Power-Off & Power-On Conditions ($M_\infty = 0.7$, $Re = 12.62 \times 10^6$).

Table 3: Drag Decomposition of Unpowered & Powered (in-trim) BLI Case Study at Various Flow Conditions.

	Unpowered					Powered					
$c_d \times 10^4$:	c_d	c_{d_p}	c_{d_τ}	$c_{d_{p_\mu}}$	$c_{d_{p_E}}$	c_d	c_{d_p}	c_{d_τ}	$c_{d_{p_\mu}}$	$c_{d_{p_E}}$	$c_{d_{p_{S_\phi}}}$
$M_\infty = 0.2$	112	33.8	78	14.9	18.9	135.7	53.2	82.5	13.4	39.6	0.2
$M_\infty = 0.5$	106.6	39.8	66.7	13.8	26	129.9	58.1	70.1	11.8	46.1	0.2
$M_\infty = 0.7$	199.3	139.3	60.1	21.2	118.1	243.9	180.1	63.8	24.4	155.3	0.4

5. CONCLUSIONS

An extension of PPF theory was made by introduction of a momentum source term, the derivation of which is briefly outlined. The implementation of the process is made possible through a user-defined transport equation which can be converted into a Poisson solver.

The extension of PPF theory is utilized to perform thrust/drag book-keeping, in which a propulsor is modelled using actuator disk theory. Actuator disk theory is coupled to the Navier-Stokes equations in a CFD solver by use of momentum and energy sources, therefore making thrust/drag book-keeping via PPFs possible.

As a pioneering study, the extended PPF theory is applied to a 2D embedded propulsion system, emulating BLI, i.e., the initial case study of Arntz & Atinault [40]. An initial comparison of two actuator disk models is made, before ultimately a Gaussian distribution is selected due to favorable numerical convergence. A comparison to the study of Arntz & Atinault is made with a good agreement between cases. The results provide an initial validation for the case study.

A PPF decomposition allows one to identify the direct near-field pressure generated from the actuator disk. All three cases produce similar propulsive pressure fields that correlate to the input thrust value. They result in little drag contribution for the given case study. Such results, combined with that of the disk model comparison, lead one to consider the impact various disk parameters may have on a decomposition. Thus a sensitivity study and further actuator disk model development would provide further insight as to the dependence of disk model accuracy on the expected aerodynamic performance.

The isolation of the actuator disk pressure allows for one to decompose the resulting secondary effects of the propulsion system. The Euler pressure, which captures viscous–inviscid interactions and shocks, is compared in power-off and power-on cases. The difference between the two is the resulting secondary effects of the given flow phenomena, and with PPF theory one can truly visualize where these changes occur in the near field.

Changes to viscous drag are much smaller than the Euler effects; however, the dissipative pressure field can also be informative. A comparison of the dissipative PPF behavior is shown in the channel, which could be useful to an aircraft designer as a means of understanding the the impact of the change in dissipation resulting from the propulsion system.

In summary, BLI and embedded propulsion systems have been treated as separate entities in which the internal and external flow is considered individually; this separation prevents one from making true power-off/power-on comparisons. Using PPF theory, the need for such flow distinctions is removed. As a result of this, there is potential for an improved feedback loop between external aerodynamicists and engine designers.

6. ACKNOWLEDGEMENTS

The authors on The Pennsylvania State University team would like to extend thanks to Mr. Albert John Abraham for his work on the actuator disk model. Further thanks is extended to the Institute for Computational and Data Sciences (ICDS) in providing both the hardware and software the simulations required.

REFERENCES

[1] L. Prandtl. Progress towards a method for the measurement of the components of the drag of a wing of finite span. Technical Report 116, National Advisory Committee for Aeronautics, 1923.

[2] A. Betz. A method for the direct determination of profile drag. *Zeitschrift für Flugtechnik und Motorluftschiffahrt*, 16:42–44, 1925.

[3] B.M. Jones, Cambridge University Aeronautics Laboratory, Aeronautical Research Council Great Britain, and Air Ministry. Aeronautical Research Committee. *The Measurement of Profile Drag by the Pitot-traverse Method*. Aeronautical Research Committee. Reports and memoranda. H.M. Stationery Office, 1936.

[4] K. Oswatitsch. Der Luftwiderstand als Integral des Entropiestromes. *Nachrichten der Akademie der Wissenschaften in Göttingen, Mathematisch-Physikalische*, 19:88–90, 1945.

[5] E. C. Maskell. Progress towards a method for the measurement of the components of the drag of a wing of finite span. Technical Report 72232, Royal Aircraft Establishment, Procurement Executive, Ministry of Defence, 1972.

[6] J. L. Steger and B. S. Baldwin. Shock waves and drag in the numerical calculation of compressible, irrotational transonic flow. *AIAA Journal*, 11(7):903–904, 1973.

[7] N. Yu, H. Chen, S. Samant, and P. E. Rubbert. Inviscid drag calculations for transonic flows. 6th Computational Fluid Dynamics Conference, AIAA Paper 1983-1928, July 1983.

[8] R.C Lock. Prediction of the drag of wings at subsonic speeds by viscous/inviscid interaction techniques. Technical report, Advisory Group For Aerospace Research And Development, 1985.

[9] D. Destarac. Investigating negative drag in grid convergence for two-dimensional euler solutions. *Journal of Aircraft*, 48(4):1468–1470, 2011.

[10] D. Destarac. Spurious far-field-boundary induced drag in two-dimensional flow simulations. *Journal of Aircraft*, 48(4):1444–1455, 2011.

[11] K. J. Fidkowski, M. A. Ceze, and P. L. Roe. Entropy-based drag-error estimation and mesh adaptation in two dimensions. *Journal of Aircraft*, 49(5):1485–1496, 2012.

[12] L. Paparone and R. Tognaccini. Computational fluid dynamics-based drag prediction and decomposition. *AIAA Journal*, 41(9):1647–1657, 2003.

[13] J. W. Sloof J. van der Vooren. *CFD-based drag prediction : state-of-the-art, theory, prospects*. Amsterdam: Nationaal Lucht- en Ruimtevaartlaboratorium, 1992.

[14] J. Z. Wu, H.-Y. Ma, and M .-De Zhou. *Vorticity and Vortex Dynamics*, page 776. 01 2006.

[15] M. Drela. Power balance in aerodynamic flows. *AIAA Journal*, 47(7):1761–1771, 2009.

[16] A. Arntz. *Civil Aircraft Aero-thermo-propulsive Performance Assessment by an Exergy Analysis of High-fidelity CFD-RANS Flow Solutions*. PhD thesis, Institut Supérieur de l'Aéronautique et de l'Espace, 2014.

[17] S. Schmitz and J. G. Coder. Inviscid circulatory-pressure field derived from the incompressible navier–stokes equations. *AIAA Journal*, 53(1):33–41, 2015.

[18] C.P. van Dam. Recent experience with different methods of drag prediction. *Progress in Aerospace Sciences*, 35(8):751–798, 1999.

[19] M. B. Giles and R. M. Cummings. Wake integration for three-dimensional flowfield computations: Theoretical development. *Journal of Aircraft*, 36(2):357–365, 1999.

[20] D. Destarac and J. Vooren. Drag/thrust analysis of jet-propelled transonic transport aircraft; definition of physical drag components. *Aerospace Science and Technology*, 8:545–556, September 2004.

[21] R. H. Liebeck. Design of the blended wing body subsonic transport. *Journal of Aircraft*, 41(1):10–25, 2004.

[22] C. A. Hall and D. Crichton. Engine Design Studies for a Silent Aircraft. *Journal of Turbomachinery*, 129(3):479–487, 07 2006.

[23] R. V. Florea, C. Matalanis, L. W. Hardin, M. Stucky, and A. Shabbir. Parametric analysis and design for embedded engine inlets. *Journal of Propulsion and Power*, 31(3):843–850, 2015.

[24] A. M. O. Smith and H. E. Roberts. The jet airplane utilizing boundary layer air for propulsion. *Journal of the Aeronautical Sciences*, 14(2):97–109, 1947.

[25] J. H. Brandau. Performance of waterjet propulsion systems- a review of the state-of-the-art. *Journal of Hydronautics*, 2(2):61–73, 1968.

[26] S. Thurston and M. S. Evanbar. Efficiency of a propulsor on a body of revolution-inducting boundary-layer fluid. *Journal of Aircraft*, 3(3):270–277, 1966.

[27] G. F. Wislicenus. Hydrodynamics and propulsion of submerged bodies. *ARS Journal*, 30(12):1140–1148, 1960.

[28] L. Serrano R. T. Kawai, D. M. Friedman. Blended wing body (bwb) boundary layer ingestion (bli) inlet configuration and system studies. Technical Report NASA/CR-2006-214534, National Aeronautics and Space Administration, 2006.

[29] D. K. Hall, A. C. Huang, A. Uranga, E. M. Greitzer, M. Drela, and S. Sato. Boundary layer ingestion propulsion benefit for transport aircraft. *Journal of Propulsion and Power*, 33(5):1118–1129, 2017.

[30] A. Uranga, M. Drela, E. M. Greitzer, D. K. Hall, N. A. Titchener, M. K. Lieu, N. M. Siu, C. Casses, A. C. Huang, G. M. Gatlin, and J. A. Hannon. Boundary layer ingestion benefit of the D8 transport aircraft. *AIAA Journal*, 55(11):3693–3708, 2017.

[31] B. T. Blumenthal, A. A. Elmiligui, K. A. Geiselhart, R. L. Campbell, M. D. Maughmer, and S. Schmitz. Computational investigation of a boundary-layer-ingestion propulsion system. *Journal of Aircraft*, 55(3):1141–1153, 2018.

[32] D. S. Sanders and P. Laskaridis. Full-aircraft energy-based force decomposition applied to boundary-layer ingestion. *AIAA Journal*, 58(10):4357–4373, 2020.

[33] M. A. Aguirre. *Exergy analysis of innovative aircraft with aero-propulsive coupling*. PhD thesis, Lille University of Sciences and Technologies, 2022.

[34] I. Berhouni, D. Bailly, and I. Petropoulos. Exergy balance extension to rotating reference frames: Application to a propeller configuration. *AIAA Journal*, 0(0):1–17, 0.

[35] S. Schmitz. Drag decomposition using partial-pressure fields in the compressible navier–stokes equations. *AIAA Journal*, 57(5):2030–2038, 2019.

[36] P. L. Hart and Sven Schmitz. Drag decomposition using partial-pressure fields: ONERA M6 wing. *AIAA Journal*, 60(5):2941–2952, 2022.

[37] P. L. Hart, C. J. Axten, M. D. Maughmer, and S. Schmitz. Drag decomposition of full aircraft configurations using partial-pressure fields. In *AIAA AVIATION 2022 Forum*, 2022.

[38] J. G. Coder and S. Schmitz. Thermodynamic decomposition of compressible wave drag in the euler equations. AIAA Aviation Forum Paper 2019-2958, 2019.

[39] P. L. Hart and S. Schmitz. Partial pressure field for airfoil wave drag. *AIAA Journal*, 60(10):5791–5804, 2022.

[40] A. Arntz and O. Atinault. Exergy-based performance assessment of a blended wing–body with boundary-layer ingestion. *AIAA Journal*, 53(12):3766–3776, 2015.

[41] S. Schmitz. *Aerodynamics of Wind Turbines: A physical basis for analysis and design*. Wiley, Hoboken, NJ, USA, 1 edition, 2020.

Thrust/drag decomposition using partial pressure fields

Hart, Pierce L.

2023-03-31

Hart PI, Mutangara NE, Sanders DS, Schmitz S. (2023) Thrust/drag decomposition using partial pressure fields. Presented at: 57th 3AF Applied Aerodynamics Conference AERO2023, 29-31 March 2023, Bordeaux, France

https://dspace.lib.cranfield.ac.uk/handle/1826/19663